Power Electronic Systems
Laboratory

IEEE Transactions on Industrial Electronics, Vol. 58, No. 11, pp. 5066-5075, November 2011.

Half-Controlled Boost Rectifier for Low-Power High-Speed Permanent-Magnet Generators

D. Krähenbühl
C. Zwyssig
J. W. Kolar

Eidgenössische Technische Hochschule Zürich
Swiss Federal Institute of Technology Zurich

Half-Controlled Boost Rectifier for Low-Power High-Speed Permanent-Magnet Generators

Daniel Krähenbühl, *Student Member, IEEE*, Christof Zwyssig, *Member, IEEE*, and Johann W. Kolar, *Fellow, IEEE*

***Abstract*—Literature reports several future portable and distributed power supplies in the watt-to-kilowatt range based on rotating machinery equipped with a variable-speed permanent-magnet generator. In order to generate a constant direct-current output voltage, an ultracompact highly efficient low-power rectifier is required. A suitable concept, i.e., the half-controlled three-phase pulsewidth-modulation boost rectifier (HCBR), is analyzed in this paper. In previous literature, there is only limited information available, particularly concerning current stresses, common-mode characteristics, and operating principles. Therefore, the HCBR topology analysis is completed in this paper. Furthermore, a novel modulation scheme improving the power electronics efficiency is proposed using space-vector analysis. The integration into a compressed-air-to-electric-power system with a generator rotating at 350 000 r/min is presented, and the measurements verify the theoretical results with an efficiency increase of 2% for the novel modulation scheme.**

***Index Terms*—Electric drives, half-controlled boost rectifier (HCBR), high-speed, permanent-magnet (PM) machines.**

I. Introduction

ULTRAHIGH-SPEED microgas and air turbines with electric output power of a couple of watts to a few kilowatts have been recently reported in literature [1]–[8]. The main applications for such systems are power supplies in consumer electronics, automobiles, aircraft and robots, portable/backup generators, as well as domestic combined heat and power units. Power density in electrical machines increases with increasing rotational speed [9]. Therefore, for the highest power density, these systems are operating at speeds between 100 000 r/min and 1 Mr/min at power levels of up to several kilowatts [10].

In addition to ultrahigh-speed microturbine generator systems, there are applications with lower speed generators. In [11], a wearable power system based on a combustion engine is presented, supplying an average of 20 W for four days (with peak power of 200 W) and has a total system weight of less than 4 kg. The system is originally developed for power supply of infantry soldier's equipment but can also be used in civil applications. In addition, mesoscale energy harvesting technologies such as small-scale wind turbines and microhydropower systems are developed for battery charging, supplying consumer electronics, or providing electricity for illumination [12]–[14].

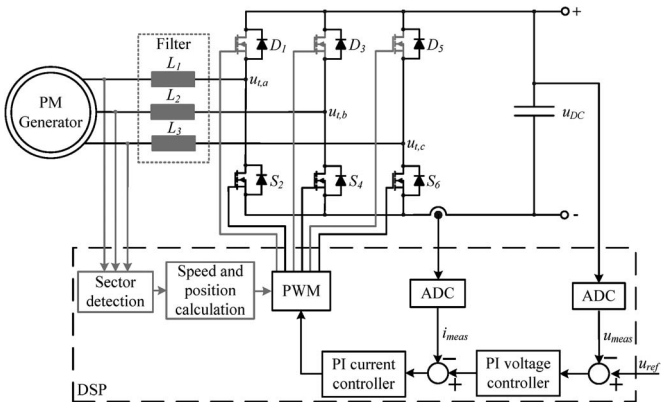

Fig. 1. HCBR $L_{1,2,3} = 3.3\ \mu$H. For the modulation scheme with synchronous switching, the sector detection must not to be implemented (gray). The high-side diodes can be exchanged with MOSFETs in order to reduce conduction losses or if bidirectional operation is required (gray).

All these systems employ a three-phase generator, usually of permanent-magnet (PM) type, operating at a variable speed depending on the load, which results in a variable three-phase output voltage [15]. However, most applications in the mentioned power range require a constant direct-current (dc) voltage, and therefore, a rectifier is required. The high fundamental phase current frequency (due to high-speed turbines and generators), the aim to build the system as compact as possible (for portable devices), and the high converter efficiency (in order not to compromise the overall system efficiency) are the main challenges. In [16]–[23], several possible one- and three-phase boost alternating-current (ac)–dc converters are summarized, and in [26], these converters have been compared concerning losses, total efficiency, volume, and control complexity. Resulting from this evaluation, the half-controlled three-phase pulsewidth-modulation (PWM) boost rectifier (HCBR) is found to be the most suitable topology for high-speed PM generators.

The HCBR (or bridgeless boost topology, cf. Fig. 1) has been introduced in [16]–[21] and as a single-phase rectifier in [22] and [23], respectively. However, in previous literature, there is only limited information available on the functional principle. Utilizing space-vector analysis, Section II shows that sinusoidal currents cannot be achieved over the entire fundamental period and that only the positive current flow can be modulated. In Section III, the standard modulation form for the HCBR is presented, followed by the space-vector

Manuscript received April 13, 2010; revised August 24, 2010, November 9, 2010, and December 18, 2010; accepted February 16, 2011. Date of publication March 10, 2011; date of current version September 7, 2011.

D. Krähenbühl and C. Zwyssig are with Celeroton AG, 8005 Zurich, Switzerland.

J. W. Kolar is with the Swiss Federal Institute of Technology Zurich, 8092 Zurich, Switzerland.

Color versions of one or more of the figures in this paper are available online at http://ieeexplore.ieee.org.

Digital Object Identifier 10.1109/TIE.2011.2126531

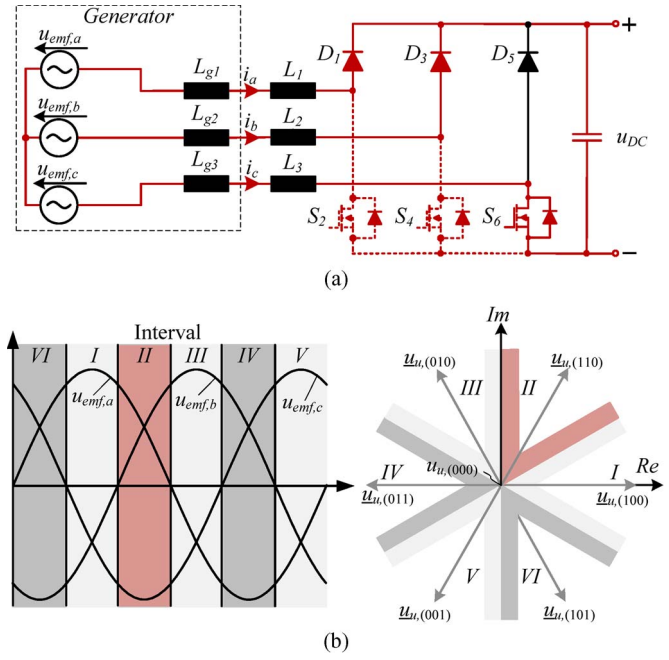

Fig. 2. Space-vector representation assuming two positive and one negative phase current, i.e., $i_a > 0$, $i_b > 0$, and $i_c < 0$ (interval *II*).

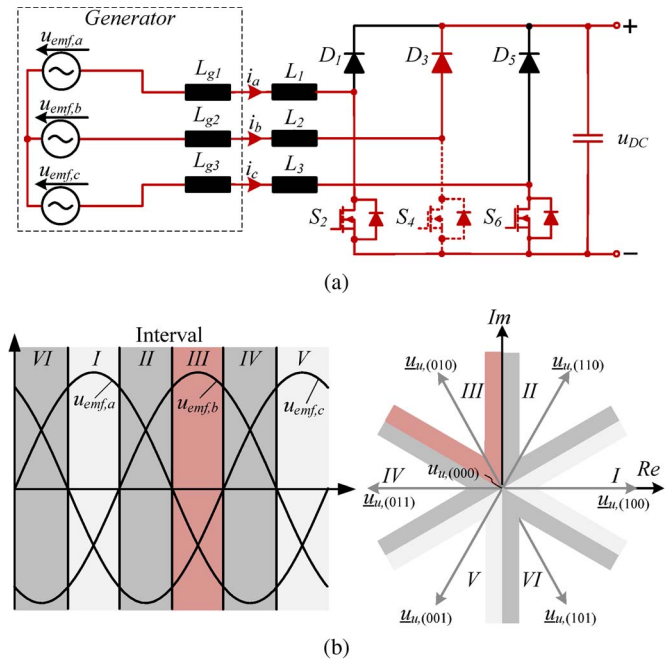

Fig. 3. Space-vector representation assuming one positive and two negative phase current, i.e., $i_a < 0$, $i_b > 0$, and $i_c < 0$ (interval *III*).

simulation, the current stresses, and the common-mode (CM) characteristics. Then, in Section IV, a novel modulation scheme is proposed, recapitulating the space-vector simulation, the current stresses, and the CM characteristics and thereby pointing out the differences and the advantages of the novel modulation scheme. Finally, the theoretical results are experimentally verified with a compressed-air-to-electric-power system (see Section IV).

II. HCBR Space-Vector Analysis

The functionality of the HCBR can be analyzed with space-vector representation of the three-phase quantities [27]. Assuming continuous conduction in all three phases and currents $i_{a,b,c}$ in phase with the back electromotive force (EMF) voltages $u_{\mathrm{emf},a,b,c}$, two different phase current conditions must be considered (see Figs. 2 and 3).

First, the condition with two positive and one negative phase current is considered, e.g., $i_a > 0$, $i_b > 0$, and $i_c < 0$ [interval *II* in Fig. 2(b)]. In this case, the current in phases a and b can flow through the diode D_1/D_3 to the high side [metal–oxide–semiconductor field-effect transistor (MOSFET) S_2/S_4 off, solid line in Fig. 2(a)] or to the negative dc rail [MOSFET S_2/S_4 on, dashed line in Fig. 2(a)], whereas the current in phase c must flow through the MOSFET S_6 or its body diode [solid line in Fig. 2(a)]. In this case, four of eight possible space vectors are available, namely, $\underline{u}_{u,(100)}$, $\underline{u}_{u,(010)}$, $\underline{u}_{u,(110)}$, and $\underline{u}_{u,(000)}$, which implies that sinusoidal currents can be formed in interval *II*. With the same approach, it can be shown that, also in intervals *IV* and *VI*, all necessary space vectors for sinusoidal current formation are also available.

Second, the condition with two negative and one positive phase current is considered, i.e., $i_a < 0$, $i_b > 0$, and $i_c < 0$ [interval *III* in Fig. 3(b)]. In this case, the current in phase b can flow through the diode D_3 to the high side [MOSFET S_4 off, solid line in Fig. 3(a)] or to the negative dc rail [MOSFET S_4 on, dashed line in Fig. 3(a)], whereas the currents in phases a and c must flow through the MOSFETs S_2/S_6 or their body diodes [solid line in Fig. 3(a)]. In this case, only two space vectors are available, namely, $\underline{u}_{u,(010)}$ and $\underline{u}_{u,(000)}$, which implies that no sinusoidal currents can be formed in interval *III*. Similarly, it can be shown that, also in intervals *I* and *V*, only two space vectors are available, and therefore, no sinusoidal currents are achievable in these intervals.

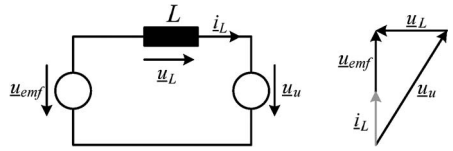

Fig. 4. Space-vector equivalent circuit and space-vector diagram of an HCBR.

Sinusoidal phase currents $\underline{i}_{a,b,c}$ in phase with $u_{\mathrm{emf},a,b,c}$ would require an average converter voltage vector $\underline{u}_u$ lagging the induced voltage vector $\underline{u}_{\mathrm{emf}}$, as shown in Fig. 4. However, if only one voltage vector besides the zero voltage vector is available, as it is the case in intervals *I*, *III*, and *V*, such an average converter voltage vector cannot be achieved, and therefore, it is impossible to achieve sinusoidal currents over the entire fundamental period, whichever modulation strategy is used. Furthermore, the space vector $\underline{u}_{u,(111)}$ cannot be applied because of the high-side diodes and the condition $i_a + i_b + i_c = 0$.

Space-vector simulations of the two modulation methods described in this paper, i.e., the standard synchronous modulation scheme and the novel sector detection scheme, are described in Sections III-A and IV-A.

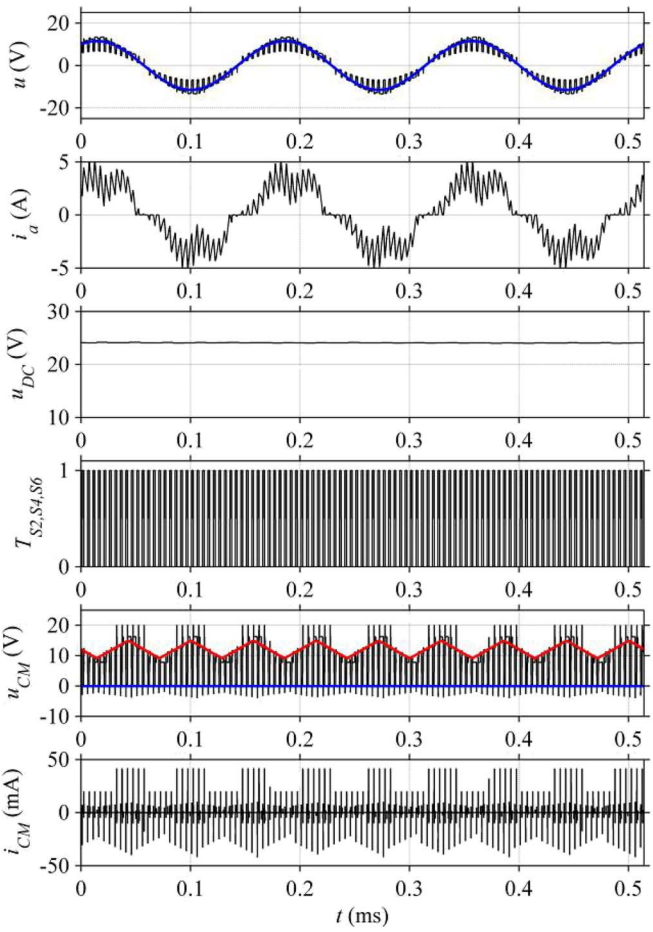

Fig. 5. Simulation results of the HCBR with the synchronous modulation scheme $L_{1,2,3} = 3.3$ μH. Generator back EMF $u_{\mathrm{emf},a}$ (blue) and terminal voltage $u_{t,a}$ (black), phase current i_a, output voltage u_{DC}, switching signals for the three-phase legs $T_{S2,S4,S6}$, as well as CM voltage u_{CM} [including the envelope, cf. (9) and (10)] and current i_{CM}, are shown. The switching frequency is $f_{\mathrm{s}} = 200$ kHz, and the fundamental frequency is $f_f = 5833$ Hz (350 000 r/min), whereas $C_{Y-\mathrm{GND}}$ was assumed to be 48 pF (cf. Fig. 7).

III. HCBR Standard Modulation Scheme

When using the standard or synchronous modulation scheme presented in [18], the same PWM signal is shared by all three switches, which leads to a short circuit of the generator phases during the turn-on interval of the PWM period that causes an increase in the currents. The generator short circuit is a valid operating state and corresponds to the space vector $\underline{u}_{u,(000)}$, as shown in Fig. 3. Simulation results for this modulation scheme can be found in Fig. 5.

The output voltage can be controlled with a cascaded voltage and current controller. To reduce complexity, the current measurement is usually implemented with a single sensor in the dc link instead of two current measurements in the generator phases. The current must therefore be measured during the off interval $(DT_s < t < T_s)$ of the PWM period, i.e., in every space-vector state except $\underline{u}_{u,(000)}$. The advantages compared with more complex modulation schemes are the lower hardware and computation effort, whereas the drawbacks are the phase current waveform cannot be controlled and losses in the diodes of the low-side MOSFETs appear, which could be omitted by turning on the respective MOSFETs.

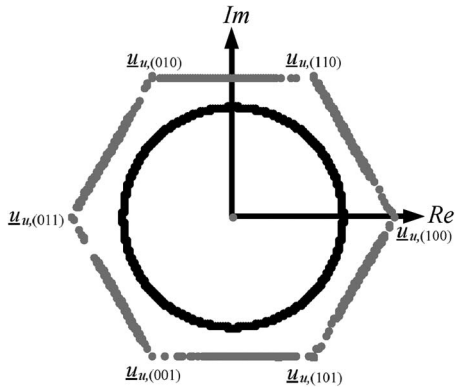

Fig. 6. Simulation of space vectors for the HCBR for the synchronous modulation scheme. (Black) Back EMF. (Gray) Terminal voltage.

A. Space-Vector Simulation for Synchronous Modulation

In Fig. 6, the simulated space vectors for the HCBR for the synchronous modulation scheme is shown. The points represent the actual impressed terminal voltage and not an average voltage. It is pointed out that not only the seven possible active space vectors are applied but also the vectors lying on the hexagon are present during the off interval of the PWM period. This is due to the floating potential of the phase that is not conducting and, therefore, is connected neither to the positive nor to the negative potential of the dc voltage. The potential of this phase changes over a 60° interval (see Fig. 9) from 0 V to u_{DC} or vice versa. This happens because the high-side diode of the phase with potential in between the values of the other two phases cannot conduct during the MOSFET's turn-off period and, therefore, changes over a 60° interval until the corresponding phase shows the highest or lowest potential for the next 120°.

B. Current Stresses for Synchronous Modulation

The losses in different components of the HCBR can be calculated with the knowledge of the according root-mean-square (RMS) currents for components with a resistive behavior or with the average currents for components with a current-independent forward voltage drop.

Assuming block-type currents, the current stresses in the high-side freewheeling diodes are independent of the modulation method and can be calculated as

$$\begin{aligned} i_{D,\mathrm{avg}} &= \hat{I}_i\,(1 - d(t)) \\ I_{D,\mathrm{avg}} &= \frac{1}{\pi}\int_{\pi/3}^{2\pi/3} \frac{\hat{I}_i}{M}\sin(\omega t)d(\omega t) = \frac{\hat{I}_i}{M\pi} \\ I_{D,\mathrm{rms}} &= \sqrt{\frac{1}{\pi}\int_{\pi/3}^{2\pi/3} \frac{\hat{I}_i^2}{M}\sin(\omega t)d(\omega t)} = \frac{\hat{I}_i}{\sqrt{M\pi}} \end{aligned} \tag{1}$$

where M is the voltage transfer ratio, i.e.,

$$M = \frac{u_{\mathrm{DC}}}{\hat{u}_{\mathrm{emf}(l-l),i}} \tag{2}$$

TABLE I
CURRENT STRESSES FOR SYNCHRONOUS MODULATION

Phase inductors	$I_{i,avg} = 0$	$I_{i,rms} = \hat{I}_i \sqrt{\frac{2}{3}}$
Freewheeling diodes	$I_{D,acg} = \frac{\hat{I}_i}{M\pi}$	$I_{D,rms} = \frac{\hat{I}_i}{\sqrt{M\pi}}$
Power MOSFETs	$I_{S,acg} = \hat{I}_i \left(\frac{2}{3} - \frac{2}{M\pi} \right)$	$I_{S,rms} = \hat{I}_i \sqrt{\frac{2}{3} - \frac{2}{M\pi}}$
Antiparallel diodes	$I_{DS,acg} = \frac{\hat{I}_i}{M\pi}$	$I_{DS,rms} = \frac{\hat{I}_i}{\sqrt{M\pi}}$
Output capacitor	$I_{C,avg} = 0$	$I_{C,rms} = \hat{I}_i \sqrt{\frac{3}{M\pi} \left(1 - \frac{3}{M\pi} \right)}$

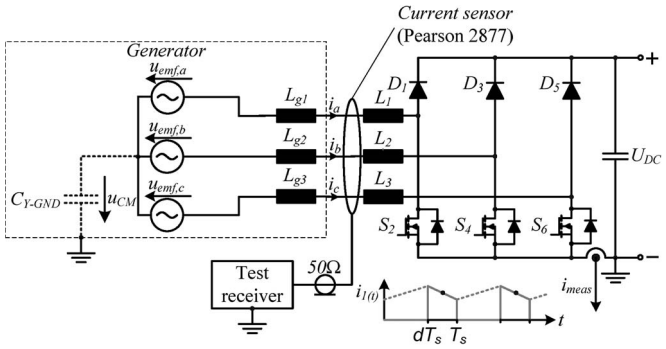

Fig. 7. Generator equivalent circuit, including the parasitic CM capacitance $C_{Y-\mathrm{GND}}$ and the HCBR. The Pearson 2877 current sensor was used to determine the CM characteristics.

where $\hat{I}_i$ is the amplitude of the block-type phase inductor currents, i.e.,

$$\hat{I}_i = I_{\mathrm{DC}} \frac{M\pi}{3} \tag{3}$$

where the duty cycle can be defined as

$$d_{(t)} = 1 - \frac{u_{\mathrm{emf}(l-l),i(t)}}{u_{\mathrm{dc}}} = 1 - \frac{1}{M} \left| \sin(\omega t) \right|. \tag{4}$$

The current stresses for the phase inductor, i.e., the power MOSFETs, the antiparallel diodes, and the output capacitor, can be calculated in a similar way [20] and are presented in Table I.

C. CM Characteristics

The HCBR is also analyzed concerning the CM characteristics according to [31]. The rectifier can be modeled as switching voltage sources. These voltage sources charge and discharge the parasitic capacitance $C_{Y-\mathrm{GND}}$ between output ground (generator casing) and generator star point (see Fig. 7), which leads to a CM noise current flow (see Fig. 8) that could disturb other sensitive electronic parts close by [23].

D. Envelope of the HF CM Voltage

Assuming $u_{\mathrm{emf},a} > u_{\mathrm{emf},b} > u_{\mathrm{emf},c}$ (sector 2 in Fig. 9), $i_a + i_b + i_c = 0$, and all three switches are in the turn-on state,

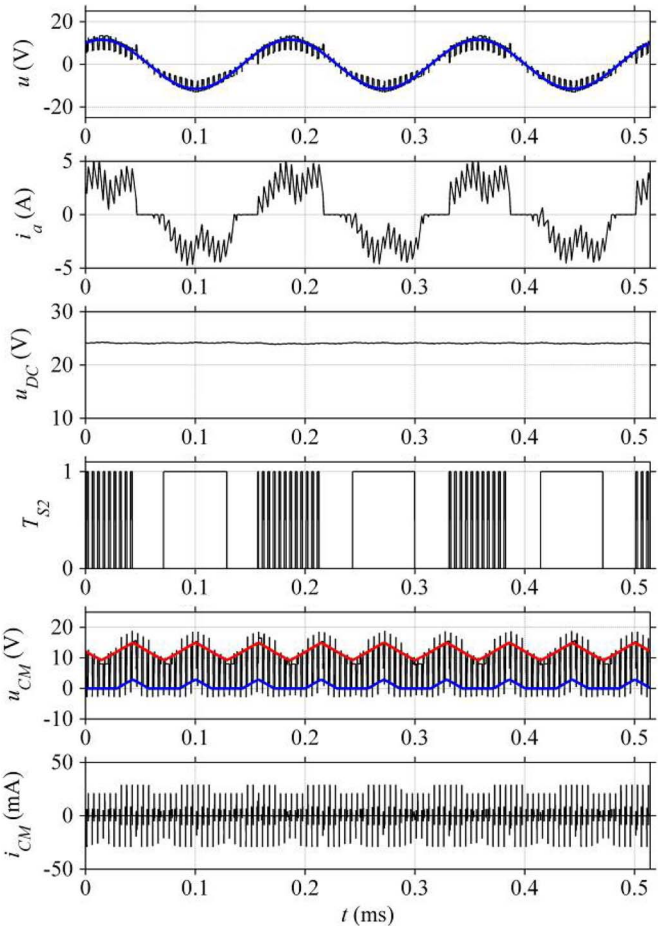

Fig. 8. Simulation results of the HCBR with the sensorless 60° sector detection modulation scheme $L_{1,2,3} = 3.3\ \mu$H. Generator back EMF $u_{\mathrm{emf},a}$ (blue) and terminal voltage $u_{t,a}$ (black), phase current i_a, output voltage u_{DC}, switching signals for one-phase leg T_{S2}, as well as CM voltage u_{CM} [including the envelope, cf. (11) and (12)] and current i_{CM}, are shown. The switching frequency is $f_s = 200$ kHz, and the fundamental frequency is $f_f = 5833$ Hz (350 000 r/min), whereas $C_{Y-\mathrm{GND}}$ was assumed to be 48 pF (cf. Fig. 7).

the CM voltage is

$$\left| \begin{array}{l} u_{\mathrm{CM}} = -u_{\mathrm{emf},a} + L\frac{di_a}{dt} \\ u_{\mathrm{CM}} = -u_{\mathrm{emf},b} + L\frac{di_b}{dt} \\ u_{\mathrm{CM}} = -u_{\mathrm{emf},c} + L\frac{di_c}{dt} \end{array} \right|$$
$$\Rightarrow 3u_{\mathrm{CM}} = -(u_{\mathrm{emf},a} + u_{\mathrm{emf},b} + u_{\mathrm{emf},c}) + L\left(\frac{di_a}{dt} + \frac{di_b}{dt} + \frac{di_c}{dt} \right) = 0$$
$$\Rightarrow u_{\mathrm{CM}} = 0. \tag{5}$$

If all three switches are turned off, the CM voltage is

$$\left| \begin{array}{l} u_{\mathrm{CM}} = -u_{\mathrm{emf},a} + L\frac{di_a}{dt} + u_{\mathrm{DC}} \\ u_{\mathrm{CM}} = -u_{\mathrm{emf},b} + L\frac{di_b}{dt} \\ u_{\mathrm{CM}} = -u_{\mathrm{emf},c} + L\frac{di_c}{dt} \end{array} \right|$$
$$\Rightarrow 3u_{\mathrm{CM}} = -(u_{\mathrm{emf},a} + u_{\mathrm{emf},b} + u_{\mathrm{emf},c}) + L\left(\frac{di_a}{dt} + \frac{di_b}{dt} + \frac{di_c}{dt} \right) + u_{\mathrm{DC}} = u_{\mathrm{DC}}$$
$$\Rightarrow u_{\mathrm{CM}} = \frac{u_{\mathrm{DC}}}{3}. \tag{6}$$

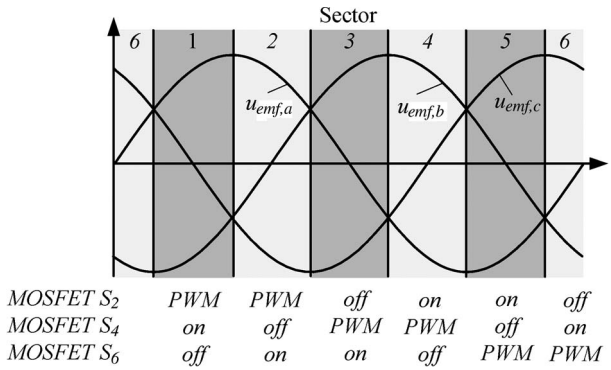

Fig. 9. Sector definitions for the HCBR and the according MOSFET states for the sector detection modulation scheme.

Still assuming $u_{\mathrm{emf},a} > u_{\mathrm{emf},b} > u_{\mathrm{emf},c}$ (sector 2 in Fig. 9) but only two conducting phases, i.e., $i_a + i_c = 0$, and all three switches are in the turn-off state, the CM voltage is

$$\left| \begin{array}{l} u_{\mathrm{CM}} = -u_{\mathrm{emf},a} + L\frac{di_a}{dt} + u_{\mathrm{DC}} \\ u_{\mathrm{CM}} = -u_{\mathrm{emf},c} + L\frac{di_c}{dt} \end{array} \right|$$

$$\Rightarrow 2u_{\mathrm{CM}} = u_{\mathrm{emf},b} + L\left(\frac{di_a}{dt} + \frac{di_c}{dt}\right) + u_{\mathrm{DC}}$$

$$\Rightarrow u_{\mathrm{CM}} = \frac{1}{2}(u_{\mathrm{emf},b} + u_{\mathrm{DC}}) \tag{7}$$

and if all three switches are turned on (but only two switches are conducting), the CM voltage is

$$\left| \begin{array}{l} u_{\mathrm{CM}} = -u_{\mathrm{emf},a} + L\frac{di_a}{dt} \\ u_{\mathrm{CM}} = -u_{\mathrm{emf},c} + L\frac{di_c}{dt} \end{array} \right|$$

$$\Rightarrow 2u_{\mathrm{CM}} = u_{\mathrm{emf},b} + L\left(\frac{di_a}{dt} + \frac{di_c}{dt}\right) = u_{\mathrm{emf},b}$$

$$\Rightarrow u_{\mathrm{CM}} = \frac{1}{2}u_{\mathrm{emf},b}. \tag{8}$$

For synchronous switching, the envelope is

$$u_{\mathrm{CM}} = 0 \qquad \text{all switches on} \tag{9}$$

$$u_{\mathrm{CM}} = \frac{1}{2}(u_{\mathrm{emf},i} + u_{\mathrm{DC}}) \qquad \text{all switches off} \tag{10}$$

as illustrated with a blue and a red curve, respectively, in Fig. 5. $u_{\mathrm{emf},i}$ is the back EMF of the phase that is not conducting and, therefore, changing every 60°.

The relevant CM capacitance $C_{Y-\mathrm{GND}}$ (see Fig. 7) has been measured for the generator presented in Section V-B with an impedance analyzer. The total capacitance of the three short-circuited phases of the generator and the generator casing is 48 pF. With this value, the CM current and voltage have been determined with simulations in GeckoCIRCUITS [32], as presented in Fig. 5.

IV. HCBR Novel Modulation Scheme

As mentioned in Section II, the current flows from the phase with the highest terminal voltage to the phase with the lowest terminal voltage, whereas the remaining phase is not conducting. This means that sharing the PWM signal with all three phases is useless for two phases. The phase sequence periodically changes every 60°; therefore, with detecting sectors 1–6, according to Fig. 9, a novel modulation scheme, which is referred to as sector detection scheme, can be realized. The sectors can be determined without a position sensor but with only measuring the machine terminal voltages [28]. In contrary to the synchronous modulation scheme, the PWM signal is now only connected to the switch of the phase showing the highest terminal voltage and, therefore, changing to the next phase every 120°. Assuming sector 1 in Fig. 9, e.g., $u_{\mathrm{emf},a} > u_{\mathrm{emf},c} > u_{\mathrm{emf},b}$, the PWM signal is connected to the switch S_2 corresponding to the phase of the highest terminal voltage $u_{\mathrm{emf},a}$, whereas the switch S_4 corresponding to the lowest terminal voltage $u_{\mathrm{emf},b}$ is continuously turned on. The terminal voltage $u_{\mathrm{emf},c}$, which lies in between the other two, does not carry any current, and therefore, the corresponding switch S_6 is turned off. This modulation scheme leads to a short circuit of the generator phases showing the highest and lowest potentials during the turn-on time of the switch, which causes an increase in the generator currents. During the turn-off time of the according switch, the current is charging the capacitor. This modulation leads to block-shaped phase currents similar to six-step brushless dc motors [29], [30]. In Fig. 8, simulation results are shown. The current amplitude variation with a frequency corresponding to six times the fundamental frequency is due to the limited bandwidth of the current controller. The output voltage can be controlled with a cascaded voltage and current controller, which is similar to the synchronous modulation scheme.

The advantages of this novel modulation scheme compared with the previously reported modulation scheme are the lower switching and conduction losses because the current in the lower switches is always flowing through the MOSFETs and not through the body diodes, and high-frequency (HF) switching only appears in one half-bridge at a time.

As a side effect, the generator speed can be calculated with the sector detection unit, which can be used for monitoring and controlling of the turbine generator system.

A. Space-Vector Simulation for the Sector Detection Scheme

In Fig. 10, the simulated space vectors for the HCBR for the sector modulation scheme is shown. In contrary to the synchronous modulation scheme, in the sector modulation scheme, the three MOSFETs are never simultaneously closed, and therefore, the space vector $\underline{u}_{u,(000)}$ is not applied. Instead of the short-circuit space vector $\underline{u}_{u,(000)}$, a vector in the direction of $\underline{u}_{u,(100)}$, $\underline{u}u,(010)$, or $\underline{u}_{u,(001)}$ is applied during the on interval of the PWM period; the amplitude varies due to the floating phase with a potential between the positive or negative potential of the dc link.

Assuming $u_{\mathrm{emf},a} > u_{\mathrm{emf},c} > u_{\mathrm{emf},b}$, e.g., sector 1 in Fig. 9, and switch S_2 is turned off during the PWM interval, and switch S_4 is continually turned on, the corresponding space vector is lying between $\underline{u}_{u,(101)}$ and $\underline{u}_{u,(100)}$ (floating phase $u_{\mathrm{emf},c}$ changing from u_{DC} to 0 V), whereas if switch S_2 is turned on during the PWM interval, the corresponding space vector

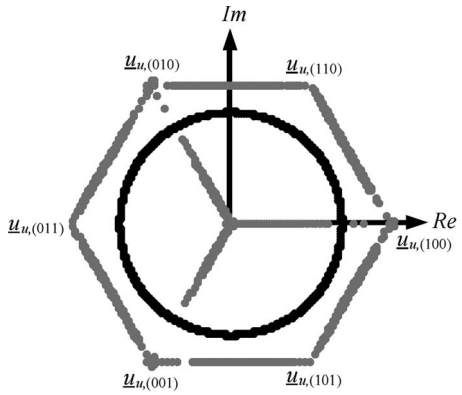

Fig. 10. Simulation of space vectors for the HCBR for the sector modulation scheme. (Black) Back EMF. (Gray) Terminal voltage.

TABLE II
CURRENT STRESSES FOR THE SECTOR DETECTION SCHEME

Phase inductors	$I_{i,avg} = 0$	$I_{i,rms} = \hat{I}_i \sqrt{\frac{2}{3}}$
Freewheeling diodes	$I_{D,acg} = \frac{\hat{I}_i}{M\pi}$	$I_{D,rms} = \frac{\hat{I}_i}{\sqrt{M\pi}}$
Power MOSFETs	$I_{S,acg} = \hat{I}_i \left(\frac{2}{3} - \frac{1}{M\pi} \right)$	$I_{S,rms} = \hat{I}_i \sqrt{\frac{2}{3} - \frac{1}{M\pi}}$
Antiparallel diodes	$I_{DS,acg} = 0$	$I_{DS,rms} = 0$
Output capacitor	$I_{C,avg} = 0$	$I_{C,rms} = \hat{I}_i \sqrt{\frac{3}{M\pi} \left(1 - \frac{3}{M\pi} \right)}$

is in the direction of $\underline{u}_{u,(001)}$ depending on the amplitude of the floating phase $u_{\mathrm{emf},c}$.

B. Current Stresses for the Sector Detection Scheme

Assuming block-type currents, Table II presents the current stresses in the phases, the power transistors [MOSFETs or insulated-gate bipolar transistors (IGBTs)], the freewheeling diodes, the antiparallel diodes, and the output capacitor of the HCBR for the sector modulation scheme. In contrary to the synchronous modulation scheme, the current stresses and losses in the antiparallel (body) diodes are zero. Due to the constant conducting state of the power switch during the 120° interval, the current stresses in the switch are higher compared with the synchronous modulation scheme. Therefore, when using the sector detection modulation scheme, the conduction current in the MOSFET or IGBT is increased by the conduction current of the antiparallel (body) diode (cf. Tables I and II). Therefore, compared with the standard modulation scheme, a MOSFET with a slightly higher current rating could be chosen. However, for a fair comparison of the two modulation schemes, the same hardware (and, therefore, silicon area) is used for both modulation schemes. However, the ohmic losses in the MOSFET ON-resistance are lower than those in the voltage drop of the body diode, and therefore, the overall losses are reduced, and this results, together with the lower switching losses, in higher system efficiency, particularly at high output power.

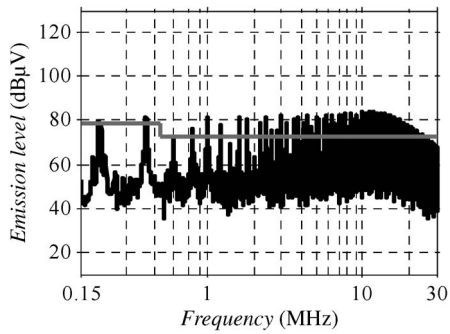

Fig. 11. Simulated quasi-peak CM conducted emission when using the synchronous modulation scheme and a switching frequency of $f_s = 200$ kHz.

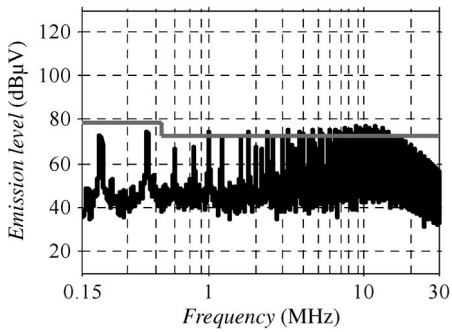

Fig. 12. Simulated quasi-peak CM conducted emission when using the sector detection modulation scheme and a switching frequency of $f_s = 200$ kHz.

C. Envelope and Simulations of the HF CM Voltage

Resulting from (5)–(8), the CM voltage envelope for sector detection modulation is

$$u_{\mathrm{CM}} = \max\left(\frac{1}{2}u_{\mathrm{emf},i}, 0\right) \qquad \text{PWM switch} = \text{on} \qquad (11)$$

$$u_{\mathrm{CM}} = \frac{1}{2}(u_{\mathrm{emf},i} + u_{\mathrm{DC}}) \qquad \text{all switches off} \qquad (12)$$

as illustrated with a blue and a red curve, respectively, in Fig. 8. $u_{\mathrm{emf},i}$ is the back EMF of the phase that is not conducting and, therefore, changing every 60°. The marginal difference compared with synchronous modulation of the CM voltage envelope is negligible and has no influence on the quasi-peak CM conducted emission measurements (cf. Figs. 13 and 14).

In Figs. 11 and 12, i.e., the simulated quasi-peak CM conducted emission for the synchronous and sector detection modulation schemes, respectively, a $C_{Y-\mathrm{GND}}$ value of 48 pF and a switching frequency of $f_s = 200$ kHz are shown. Considering the rough model of the CM behavior, simulations (see Figs. 11 and 12) and measurements (see Figs. 13 and 14) are in good agreement. In addition, simulations and measurements with a switching frequency of $f_s = 400$ kHz are in good agreement.

V. MEASUREMENTS

A. Experimental Setup

In [8], a miniature compressed-air-to-electric-power system, which is based on a single-stage axial impulse turbine with a rated rotational speed of 350 000 r/min and a rated electric

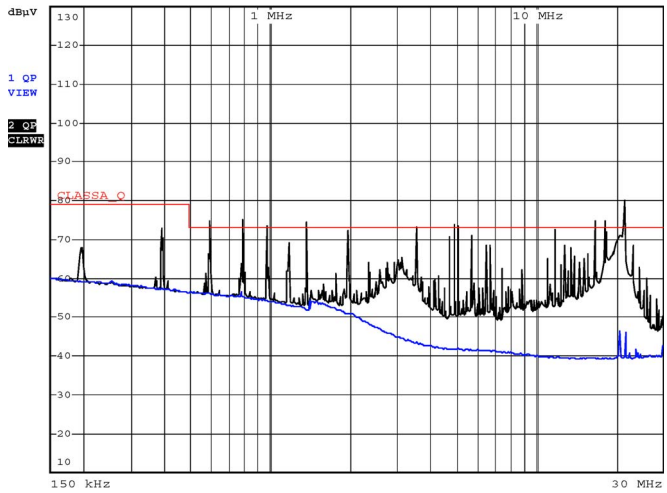

Fig. 13. Measured quasi-peak CM conducted emission when using the synchronous modulation scheme and a switching frequency of $f_s = 200$ kHz. The CM component of the input currents is measured with a current probe Pearson 2877 in order to obtain only the CM signal. The blue signal represents the quasi-peak noise floor.

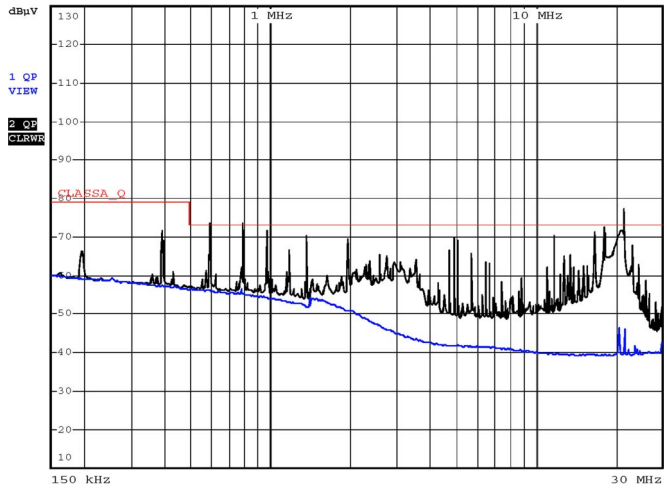

Fig. 14. Measured quasi-peak CM conducted emission when using the sector detection modulation scheme and a switching frequency of $f_s = 200$ kHz. The CM component of the input currents is measured with a current probe Pearson 2877 in order to obtain only the CM signal. The blue signal represents the quasi-peak noise floor.

TABLE III
GENERATOR DATA

parameter	description	value	Unit
n_{max}	maximum speed	500 000	Rpm
n_r	rated speed	350 000	Rpm
Ψ_{PM}	magnet flux linkage	0.32	mVs
L_S	stator inductance	2.1	µH
R_S	stator resistance	0.12	Ω

power output of 60 W, is presented. With a passive resistive three-phase load, a maximum electric output power value of 124 W at 370 000 r/min has been experimentally determined. In Table III, the measured generator data are compiled. This system has been used to experimentally characterize the rectifier that has been theoretically analyzed in this paper.

The experimental setup of the HCBR is shown in Fig. 15. The main power devices are MOSFETs (IRF6644 DirectFET) and diodes (IR 12CWQ03FNPbF), as well as three ac inductors (Vishay–Dale IHLP2525CZER2R2M01) when using a switching frequency of 200 kHz. The switching frequency is chosen such that the current ripple is 2 A. Only relying on the generator inductance, this leads to a switching frequency of 400 kHz; with additional ac inductors, the total inductance can be doubled, and the switching frequency can be reduced to 200 kHz when allowing for the same current ripple of 2 A.

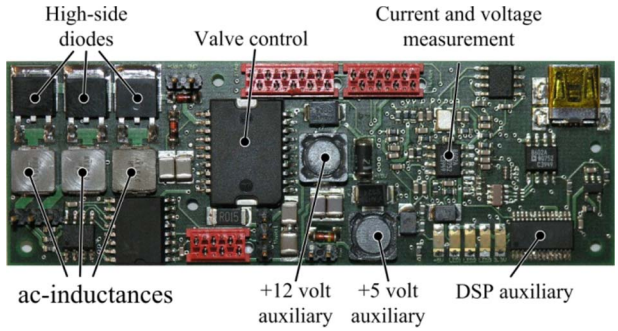

Fig. 15. HCBR electronics, including the valve control electronics (90 mm × 30 mm × 9 mm). Used power devices: MOSFETs (IRF6644 DirectFET), diodes (IR 12CWQ03FNPbF), and ac inductors (Vishay–Dale IHLP2525CZER2R2M01).

The same hardware has been used for all measurements, e.g., when using the higher switching frequency (400 kHz), no additional ac filter inductors have to be used. They are bypassed on the hardware by directly soldering the motor phases to the drain of the MOSFETs. Only the motor inductors are used in this configuration method. For a switching frequency of 200 kHz, the total phase inductance (internal generator inductance plus external ac inductors) must be higher (in order to have the same current ripple), and therefore, the ac inductors are not bypassed. Further details about the experimental setup can be found in [26].

B. CM Measurements

In order to verify the proposed CM propagation model and the simulation shown in Fig. 12, CM measurements have been carried out, employing an HF current probe Pearson 2877 with a nominal bandwidth of 200 MHz.

The current sensor produces an output signal of 1 V/A at an external 50-Ω termination, (which lies in parallel to the internal 50-Ω termination of the sensor), which corresponds to an attenuation G_{Pearson} of

$$G_{\text{Pearson}} = 20 \cdot \log(1) = 0 \text{ dB}. \tag{13}$$

The measurement at the line impedance stabilization network (LISN) equivalent input resistance $R_{\text{LISN}}/3 = 50\ \Omega/3$ appears with a gain G_{LISN} of

$$G_{\text{LISN}} = 20 \cdot \log(50/3) = 24.4 \text{ dB}. \tag{14}$$

Therefore, the gain of the measurement result with the Pearson 2877 current sensor G_{total} is given by

$$G_{\text{total}} = G_{\text{LISN}} - G_{\text{Pearson}} = 24.4 \text{ dB}. \tag{15}$$

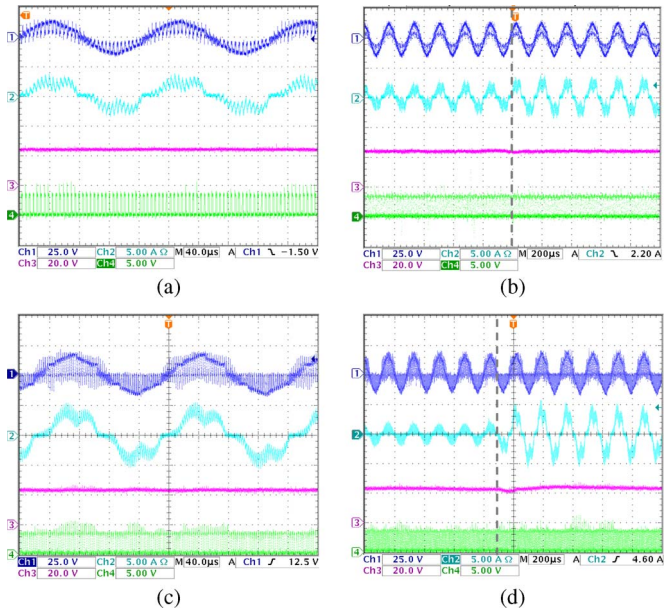

Fig. 16. Measurement results of the HCBR with the synchronous modulation scheme at 350 000 r/min, switching frequencies of (a)/(b) $f_s = 200$ kHz and (c)/(d) $f_s = 400$ kHz, and output power values of (a) 40 W and (c) 50 W, as well as (dashed vertical line) output power step changes of (b) from 15 to 40 W and (d) from 15 to 50 W. (Channel 1) Terminal voltage. (Channel 2) Phase current. (Channel 3) Output voltage. (Channel 4) PWM signal for all three switches.

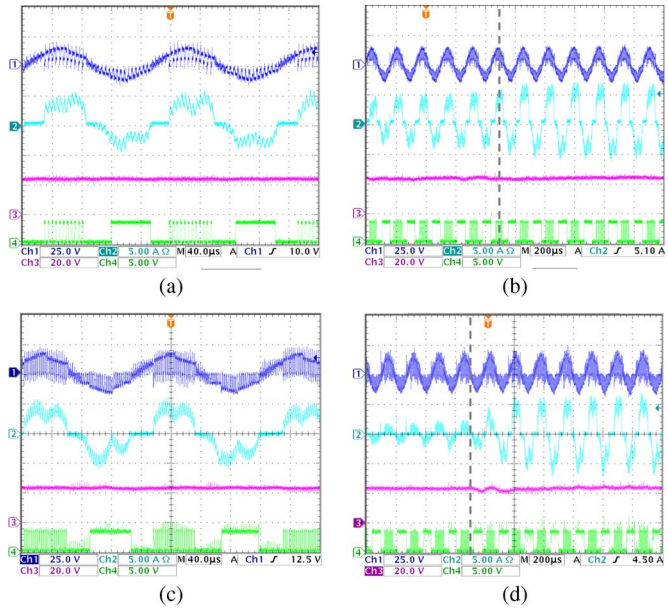

Fig. 17. Measurement results of the HCBR with the sector detection modulation scheme at 350 000 r/min, switching frequencies of (a)/(b) $f_s = 200$ kHz and (c)/(d) $f_s = 400$ kHz, and output power of (a)/(c) 50 W, as well as (dashed vertical line) output power step changes of (b) from 30 to 60 W and (d) from 15 to 75 W. (Channel 1) Terminal voltage. (Channel 2) Phase current. (Channel 3) Output voltage. (Channel 4) PWM signal for one switch.

Accordingly, the actual measurements are 24.4 dB below the measurements detected by an electromagnetic compatibility test receiver. Therefore, this correction factor has to be considered for the conducted emission measurement presented.

In Fig. 14, a quasi-peak CM conducted emission measurement when using sector detection modulation and a switching frequency of $f_s = 200$ kHz is shown, whereas in Fig. 13, a quasi-peak CM conducted emission measurement when using synchronous modulation and a switching frequency of $f_s = 200$ kHz is presented. The measurements have been carried out with a spectrum analyzer with input impedance of 50 Ω. The first peak at 200 kHz is related to the rectifier switching frequency.

The standard International Special Committee on Radio Interference (CISPR) 11 was chosen for establishing the performance requirements, where the frequency range of 0.15–30 MHz is considered for class-A equipment. The limits for this are represented through a red curve in Figs. 12–14.

C. Waveform and Efficiency Measurements

In Figs. 16(a)/(c) and 17(a)/(c), measurements with an HCBR at 350 000 r/min and switching frequencies of 200 and 400 kHz are shown. With the sector detection modulation scheme (see Fig. 17), the 120° block-type waveform for positive phase current and the rather high current ripple of approximately 2 A can be seen, whereas the waveform for the modulation scheme with the synchronous modulation scheme (see Fig. 16) slightly differs from a 120° block type for positive phase current. All measurements show good agreement with the simulation results in Figs. 5 and 8, respectively. In Figs. 16(b)/(d) and 17(b)/(d), a load step on the dc side and the resulting dc voltage and phase current waveforms are shown. In Fig. 18, simulated and measured efficiency values of the HCBR with the sector detection and synchronous modulation schemes at different output power levels and different switching frequencies are presented. Using a higher switching frequency instead of additional ac inductors increases the efficiency by up to 3% at high output power levels and reduces the total inverter volume. Compared with the standard modulation scheme, the novel sector detection modulation scheme results in an efficiency increase of about 2% over the entire operating area.

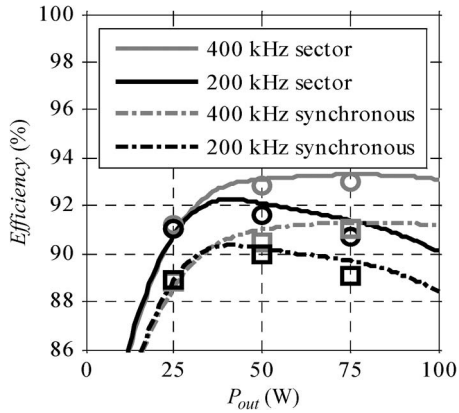

Fig. 18. Comparison of (lines) simulated and (circles/squares) measured efficiency values with the HCBR with the (circles) sector detection modulation scheme and (squares) synchronous modulation scheme at different output power levels and different switching frequencies.

VI. Conclusion

The HCBR is an ideal choice for an interface between a variable-speed PM generator and a constant dc output voltage.

In this paper, the previously missing analysis on the HCBR has been provided, including the space-vector representation, the current stresses, and the CM characteristics.

With a novel modulation scheme referred to as the sector detection modulation scheme, both switching and conduction losses in the semiconductors can be lowered, and therefore, the power electronics efficiency is increased. In an experimental setup, this results in an efficiency increase of approximately 2% over the entire operating range. Further experimental results show that increasing the switching frequency can result in a higher total efficiency value because additional ac inductors (and, therefore, their losses) can be omitted. The novel control strategy is not limited to low-power high-speed permanent magnet generators and could be implemented in various applications were an HCBR is used.

REFERENCES

[1] M. Morimoto, K. Aiba, T. Sakurai, A. Hoshino, and M. Fujiwara, "Position sensorless starting of super high-speed PM generator for micro gas turbine," *IEEE Trans. Ind. Electron.*, vol. 53, no. 2, pp. 415–420, Apr. 2006.

[2] L. G. Frechette, S. A. Jacobson, K. S. Breuer, F. F. Ehrich, R. Ghodssi, R. Khanna, C. W. Wei Wong, X. Zhang, M. A. Schmidt, and A. H. Epstein, "Demonstration of a microfabricated high-speed turbine supported on gas bearings," in *Proc. Solid State Sens. Actuator Workshop*, Hilton Head Island, SC, 2000.

[3] J. Peirs, D. Reynaerts, and F. Verplaetsen, "A microturbine for electric power generation," *Sens. Actuators A, Phys.*, vol. 113, no. 1, pp. 86–93, June 2004.

[4] S. Tanaka, K. Hikichi, S. Togo, M. Murayama, Y. Hirose, T. Sakurai, S. Yuasa, S. Teramoto, T. Niino, T. Mori, M. Esashi, and K. Isomura, "World's smallest gas turbine establishing Brayton cycle," in *Proc. 7th Int. Workshop PowerMEMS*, Freiburg, Germany, Nov. 27–29, 2007, pp. 359–362.

[5] D. P. Arnold, F. Herrault, I. Zana, P. Galle, J.-W. Park, S. Das, J. H. Lang, and M. G. Allen, "Design optimization of an 8-Watt, microscale, axial-flux, permanent-magnet generator," *J. Micromech. Microeng.*, vol. 16, no. 9, pp. 290–296, Sep. 2006.

[6] B. C. Yen, F. Herrault, K. J. Hillman, M. G. Allen, F. F. Ehrich, S. Jacobson, C. H. Ji, J. H. Lang, H. Li, Z. S. Spakovszky, and D. R. Veazie, "Characterization of a fully-integrated permanent-magnet turbine generator," in *Proc. 8th Int. Workshop PowerMEMS*, Sendai, Japan, Nov. 9–12, 2008, pp. 121–124.

[7] H. Raisigel, O. Cugat, and J. Delamare, "Permanent magnet planar micro-generators," *Sens. Actuators A, Phys.*, vol. 130–131, pp. 438–444, Aug. 2006.

[8] D. Krähenbühl, C. Zwyssig, H. Hörler, and J. W. Kolar, "Design considerations and experimental results of a 60 W compressed-air-to-electric-power system," in *Proc. IEEE/ASME Int. Conf. MESA*, Beijing, China, Oct. 12–15, 2008, pp. 375–380.

[9] A. Binder and T. Schneider, "High-speed inverter-fed AC drives," in *Proc. Int. Aegean Conf. Elect. Mach. Power Electron., Electromotion*, Bodrum, Turkey, Sep. 10-12, 2007, pp. 9–16.

[10] A. Borisavljevic, H. Polinder, and J. A. Ferreira, "On the speed limits of permanent-magnet machines," *IEEE Trans. Ind. Electron.*, vol. 57, no. 1, pp. 220–227, Jan. 2010.

[11] I. Kovacevic, S. D. Round, J. W. Kolar, and K. Boulouchos, "Optimization of a wearable power system," in *Proc. 11th Workshop COMPEL*, Aug. 17–20, 2008, pp. 1–6.

[12] J. M. Carrasco, L. G. Franquelo, J. T. Bialasiewicz, E. Galvan, R. C. Portillo Guisado, M. A. M. Prats, J. I. Leon, and N. Moreno-Alfonso, "Power-electronic systems for the grid integration of renewable energy sources: A survey," *IEEE Trans. Ind. Electron.*, vol. 53, no. 4, pp. 1002–1016, Jun. 2006.

[13] G. Boyle, Ed., *Renewable Energy: Power for a Sustainable Future*. London, U.K.: Oxford Univ. Press, 1996.

[14] [Online]. Available: http://www.solarwindworks.com

[15] P. D. Pfister and Y. Perriard, "Very-high-speed slotless permanent-magnet motors: Analytical modeling, optimization, design, and torque measurement methods," *IEEE Trans. Ind. Electron.*, vol. 57, no. 1, pp. 296–303, Jan. 2010.

[16] J. Kikuchi, M. D. Manjrekar, and T. A. Lipo, "Performance improvement of half controlled 3-phase PWM boost rectifier," in *Proc. 30th Annu. IEEE Power Electron. Spec. Conf.*, 1999, vol. 1, pp. 319–324.

[17] J. Kikuchi, M. D. Manjrekar, and T. A. Lipo, "Complementary half controlled three phase PWM boost rectifier for multi-DC-link applications," in *Proc. 15th Annu. IEEE APEC*, 2000, vol. 1, pp. 494–500.

[18] D. J. Perreault and V. Caliskan, "Automotive power generation and control," *IEEE Trans. Power Electron.*, vol. 19, no. 3, pp. 618–630, May 2004.

[19] J. M. Rivas, D. J. Perreault, and T. A. Keim, "Performance improvement in alternators with switched-mode rectifiers," *IEEE Trans. Energy Convers.*, vol. 19, no. 3, pp. 561–568, Sep. 2004.

[20] J. Miniböck, "Dreiphasen dreischalter dreipunkt pulsgleichrichtersystem," Ph.D. dissertation, Swiss Federal Inst. Technol. Zurich, Zurich, Switzerland, 2008.

[21] J. C. Salmon, "Circuit topologies for PWM boost rectifiers operated from 1-phase and 3-phase ac supplies and using either single or split dc rail voltage outputs," in *Proc. IEEE Appl. Power Electron. Conf.*, Mar. 1995, pp. 473–479.

[22] L. Huber, Y. Jang, and M. Jovanovic, "Performance evaluation of bridgeless PFC boost rectifier," *IEEE Trans. Power Electron.*, vol. 23, no. 3, pp. 1381–1390, May 2008.

[23] J. R. Rodriguez, J. W. Dixon, J. R. Espinoza, J. Pontt, and P. Lezana, "PWM regenerative rectifiers: State of the art," *IEEE Trans. Ind. Electron.*, vol. 52, no. 1, pp. 5–22, Feb. 2005.

[24] Y. Jang and M. M. Jovanovic, "A bridgeless PFC boost rectifier with optimized magnetic utilization," *IEEE Trans. Power Electron.*, vol. 24, no. 1, pp. 85–93, Jan. 2009.

[25] H. Ye, Z. Yang, J. Dai, C. Yan, X. Xin, and J. Ying, "Common mode noise modeling and analysis of dual boost PFC circuit," in *Proc. 26th IEEE Int. Telecommun. Energy Conf.*, Sep. 19–23, 2004, pp. 575–582.

[26] D. Krähenbühl, C. Zwyssig, K. Bitterli, M. Imhof, and J. W. Kolar, "Evaluation of ultra-compact rectifiers for low power, high-speed, permanent-magnet generators," in *Proc. 35th IEEE IECON*, Porto, Portugal, Nov. 3–5, 2009, pp. 448–455.

[27] M. Malinowski, M. Jasinski, and M. P. Kazmierkowski, "Simple direct power control of three-phase PWM rectifier using space-vector modulation (DPC-SVM)," *IEEE Trans. Ind. Electron.*, vol. 51, no. 2, pp. 447–454, Apr. 2004.

[28] P. P. Acarnley and J. F. Watson, "Review of position-sensorless operation of brushless permanent-magnet machines," *IEEE Trans. Ind. Electron.*, vol. 53, no. 2, pp. 352–362, Apr. 2006.

[29] K. Iizuka, H. Uzuhashi, M. Kano, T. Endo, and K. Mohri, "Microcomputer control for sensorless brushless motor," *IEEE Trans. Ind. Appl.*, vol. IA-21, no. 3, pp. 595–601, May 1985.

[30] C. Zwyssig, S. D. Round, and J. W. Kolar, "An ultrahigh-speed, low power electrical drive system," *IEEE Trans. Ind. Electron.*, vol. 55, no. 2, pp. 577–585, Feb. 2008.

[31] J.-S. Lai, X. Huang, E. Pepa, S. Chen, and T. W. Nehl, "Inverter EMI modeling and simulation methodologies," *IEEE Trans. Ind. Electron.*, vol. 53, no. 3, pp. 736–744, Jun. 2006.

[32] [Online]. Available: http://www.gecko-research.com

Daniel Krähenbühl (S'08) received the M.Sc. and Ph.D. degrees in electrical engineering from the Swiss Federal Institute of Technology Zurich, Zurich, Switzerland, in 2007 and 2010, respectively.

In 2007, he concluded his M.Sc. thesis, in which he designed and realized a 1.5-kW converter for bearingless motors, in cooperation with Levitronix GmbH. His Ph.D. research focused on ultrahigh-speed electrically driven turbocompressors and turbine generator systems and their power electronics. Since June 2010, he has been with Celeroton AG, Zurich, a spin-off company in the area of high-speed electrical drive systems. His research interests include mechatronics, power electronics, and microelectronics.

Christof Zwyssig (M'10) received the M.Sc. and Ph.D. degrees in electrical engineering from the Swiss Federal Institute of Technology Zurich, Zurich, Switzerland, in 2004 and 2008, respectively.

He was with Chalmers University of Technology, Gothenburg, Sweden, where he was involved in the field of wind turbines. Since January 2009, he has been with Celeroton AG, Zurich, a spin-off company in the area of high-speed electrical drive systems, of which he is a cofounder. He studied power electronics, machines, and magnetic bearings and was engaged in research on high-speed electrical drive systems and their power electronics.

Johann W. Kolar (F'10) received the M.Sc. and Ph.D. degrees (*summa cum laude/promotio sub auspiciis praesidentis rei publicae*) from Vienna University of Technology, Vienna, Austria.

Since 1984, he has been an independent international consultant in close collaboration with Vienna University of Technology in the fields of power electronics, industrial electronics, and high-performance drives. He proposed numerous novel pulsewidth-modulation converter topologies, as well as modulation and control concepts, e.g., the Vienna rectifier and the three-phase alternating-current (ac)–ac sparse matrix converter. On February 1, 2001, he was appointed Professor and Head of the Power Electronic Systems Laboratory, Swiss Federal Institute of Technology (ETH) Zurich, Zurich, Switzerland. He is the author or coauthor of more than 350 scientific papers published in international journals and conference proceedings. HE is the holder of more than 75 patents. His current research focuses on ac–ac and ac–direct-current converter topologies with low effects on the mains, e.g., for power supply of data centers, more electric aircraft, and distributed renewable energy systems. Furthermore, the main areas of his research are the realization of ultracompact and ultraefficient converter modules employing latest power semiconductor technology (SiC and GaN), novel concepts for cooling and electromagnetic interference filtering, multidomain/multiscale modeling/simulation and multiobjective optimization, physical model-based lifetime prediction, pulsed power, and ultrahigh-speed and bearingless motors.

Dr. Kolar is a member of the Institute of Electrical Engineers of Japan (IEEJ). He is a member of the international steering and technical program committees of numerous international conferences in the field (e.g., Director of the Power Quality Branch of the International Conference on Power Conversion and Intelligent Motion). He is the founding Chairman of the IEEE Power Electronics Society (PELS) Austria and Switzerland Chapters and the Chairman of the Education Chapter of the European Power Electronics and Drives Association. From 1997 to 2000, he served as an Associate Editor of the IEEE TRANSACTIONS ON INDUSTRIAL ELECTRONICS. Since 2001, he has been an Associate Editor of the IEEE TRANSACTIONS ON POWER ELECTRONICS. Since 2002, he has also been an Associate Editor of the *Journal of Power Electronics* of the Korean Institute of Power Electronics and a member of the Editorial Advisory Board of the *IEEJ Transactions on Electrical and Electronic Engineering*. He was a recipient of the Best Transactions Paper Award from the IEEE Industrial Electronics Society (IES) in 2005, the Best Paper Award at the International Conference on Power Electronics in 2007, the 1st Prize Paper Award from the IEEE Industry Applications Society Industrial Power Converter Committee in 2008, the IEEE Industrial Electronics Conference Best Paper Award from the IES Power Electronics Technical Committee in 2009, the 2009 PELS Transaction Prize Paper Award, and the 2010 Best Paper Award of the *IEEE/ASME Transactions on Mechatronics*. He also received an Erskine Fellowship from the University of Canterbury, Christchurch, New Zealand, in 2003. He initiated and/or is the founder/cofounder of four spin-off companies targeting ultrahigh-speed drives, multidomain/multilevel simulation, ultracompact/ultraefficient converter systems, as well as pulsed-power and electronic energy processing. In 2006, the European Power Supplies Manufacturers Association awarded the Power Electronics Systems Laboratory of ETH Zurich as the leading academic research institution in Power Electronics in Europe.